Single-molecule study of the dynamic organization of Vascular Endothelial Growth Factor Receptor 2 on the endothelial cell surface

Bruno da Rocha-Azevedo[a], Sungsoo Lee[a,1], Aparajita Dasgupta[a], Anthony R. Vega[a,b], Luciana R. de Oliveira[a], Tae Kim[a], Mark Kittisopikul[a,1] and Khuloud Jaqaman[a,b,2]

[a] Department of Biophysics, UT Southwestern Medical Center, Dallas, TX, 75390, United States.

[b] Lyda Hill Department of Bioinformatics, UT Southwestern Medical Center, Dallas, TX, 75390, United States.

[1] Current addresses: S.L.: Department of Life Sciences, Korea University, Seoul, South Korea; M.K.: Department of Cell and Developmental Biology, Northwestern University Feinberg School of Medicine, Chicago, IL, United States.

[2] Corresponding author: Khuloud Jaqaman; Department of Biophysics, UT Southwestern Medical Center, Dallas, TX, 75390, United States; 214-645-9752; khuloud.jaqaman@utsouthwestern.edu.

Keywords: VEGFR-2, VEGFR2, live-cell imaging, receptor tyrosine kinase, spatiotemporal organization, angiogenesis.

Abstract

There is growing evidence that receptors exhibit dynamic, nanoscale organization on the cell surface, which plays an important role in their signaling function. Vascular Endothelial Growth Factor (VEGF) Receptor 2 (VEGFR-2) is a critical Receptor Tyrosine Kinase in endothelial cells, where it initiates signaling cascades that promote angiogenesis. Little is known about the nanoscale organization of VEGFR-2 on the endothelial cell surface and how it influences VEGF binding and subsequent signaling. To fill this gap in our knowledge, we performed live-cell single-molecule imaging of endogenous VEGFR-2 in primary endothelial cells, followed by a pipeline of automated image analysis and multiscale data analysis to quantitatively characterize and extract relationships between VEGFR-2 mobility, interactions, phosphorylation and ligand binding. We found that surface VEGFR-2 in unstimulated cells can be mobile or immobile/confined, both of which can be monomeric or non-monomeric, with a complex interplay between mobility and inter-receptor interactions. The immobile/confined mode depends on VEGFR-2 phosphorylation, even in unstimulated cells, and is enriched further in the presence of VEGF. Co-imaging of VEGFR-2 and labeled VEGF allowed us to test two models of VEGFR-2 activation, namely VEGF-induced dimerization versus VEGF binding to pre-existing dimers. We found evidence for both models, with stronger evidence for binding and stabilizing pre-existing dimers. Our study is the first to characterize the dynamic nanoscale organization of VEGFR-2 in its native plasma membrane environment; further investigations of the mechanisms that regulate it and its role in VEGFR-2 signaling will be critical for a more complete understanding of angiogenic signaling.

Significance Statement

Vascular Endothelial Growth Factor Receptor 2 (VEGFR-2) is a critical receptor on the surface of endothelial cells (which line the blood vessels). It promotes the formation of new blood vessels in response to its ligand VEGF. Currently we know little about the organization and dynamics of this receptor on the cell surface, with multiple proposed models regarding its activation mechanism by VEGF. To fill this knowledge gap, we conducted a quantitative single-molecule imaging study of endogenous VEGFR-2 in primary endothelial cells, revealing the dynamic nanoscale organization of VEGFR-2 in its native environment. Our study also addresses the interplay between this organization, ligand binding and receptor activation, shedding light on the cell biophysical properties of this developmentally important receptor.

Introduction

Angiogenesis, the formation of new blood vessels from the existing vasculature, is critical for physiological events such as embryo and organ development and wound healing, and in pathological states such as cancer and diabetes (1, 2). Vascular endothelial growth factor A (commonly referred to as VEGF) is the major promoter of angiogenesis in both health and disease (3, 4). VEGF Receptor 2 (VEGFR-2) on the surface of endothelial cells (ECs) is a major transducer of VEGF signals, resulting in stimulation of cell sprouting, proliferation and migration, thus promoting angiogenesis (4-8).

VEGFR-2 is a receptor tyrosine kinase (RTK). The classic model of VEGFR-2 activation by its ligand has been that VEGF binds to VEGFR-2 monomers, leading to their dimerization, then trans-autophosphorylation of their intracellular kinase domains, and thus activation and downstream signaling (7, 9). However, as for some other RTKs (10-14), recent work provides evidence that VEGFR-2 can dimerize in the absence of ligand, and VEGF binding leads to dimer conformational changes that enable receptor trans-activation (15). Interestingly, VEGF has been observed to bind more avidly to VEGFR-2 pre-dimers (16, 17). In addition, VEGFR-2 can be activated by fluid shear stress in a ligand-independent manner (18-20), raising the possibility of ligand-independent dimerization to enable activation, as dimerization is a prerequisite for the activation of many RTKs to relieve auto-inhibition (21).

Little is known about the organization of VEGFR-2 in its native EC plasma membrane environment. Yet this organization might play an important role in VEGFR-2 function, as shown for a variety of other receptors and membrane-associated proteins (22-27). To fill this knowledge gap, we performed live-cell single-molecule imaging (28, 29) followed by a pipeline of automated image analysis and multiscale data analysis to investigate the dynamic organization of endogenous

VEGFR-2 on the surface of primary ECs, and the interplay between this organization and VEGF binding and subsequent VEGFR-2 activation.

Results

VEGFR-2 exhibits mobility and organization heterogeneity on the surface of unstimulated primary human dermal microvascular ECs (HDMECs)

In order to image individual endogenous VEGFR-2 molecules, we labeled early passage primary HDMECs with a low concentration of primary anti-VEGFR-2 EIC-Fab fragments, which bound to the extracellular domain of the receptor without interfering with receptor activation (Fig. S1), followed by secondary Fab fragments conjugated to Rhodamine Red-X (RRX). Total internal reflection fluorescence microscopy (TIRFM) was then used to acquire 10 Hz/20 s imaging streams at 37°C focused on the bottom surface of the cell (Fig. 1A; Movie 1), followed by multiple-particle detection and tracking to obtain the labeled receptor trajectories, including merging and splitting events between the labeled receptors (30) (Movie 2).

Diffusion analysis (31) of each VEGFR-2 track revealed a bimodal distribution of diffusion coefficients (Fig. 1B, C; Movie 3), where ~35% of the tracks were highly mobile, with a mean diffusion coefficient of 0.0185 $\mu m^2/s$, and the remaining ~65% were much less mobile (mode termed immobile/confined (imm/conf)), with a mean diffusion coefficient of 0.008 $\mu m^2/s$. We also noticed that not all detected particles had the same intensity (Fig. 1A), suggesting that VEGFR-2 was not purely in a monomeric state in unstimulated cells. These non-monomeric states could be unligated dimers (15) or oligomers (as observed for other RTKs (13, 14)), complexes formed through interactions with other receptors (7), or clusters within nanodomains such as clathrin-

coated pits (32) or caveolae (33). As we do not know the mechanisms generating non-monomeric states, we will use the term "assembly state" for neutrality.

Deriving the apparent assembly state *n* of the tracked VEGFR-2 particles from their intensities and sequence of merging and splitting events (30, 34) revealed a distribution of states, which was interestingly mobility mode dependent (Fig. 1D). While a large fraction of the tracked particles had $n = 1$, confirming that VEGFR-2 labeling and imaging were at the single-molecule level, a substantial fraction had $n \geq 2$. Of note, because ~20% of the secondary Fab fragments had two fluorophores (Fig. 1D, highly diluted labeling), this analysis could not reveal the absolute assembly state of a detected particle. However, the fraction of VEGFR-2 with $n \geq 2$ was 41% for mobile particles and 48% for imm/conf particles, both significantly greater than 20% (p-value < 10^{-15}; Fig. 1D).

These analyses indicate that VEGFR-2 at rest, in unstimulated HDMECs, exhibits heterogeneity in both mobility and assembly state, with imm/conf molecules in higher assembly states than mobile molecules. Because of the sub-stoichiometric labeling inherent to single-molecule imaging, our analysis most likely reveals only the lower bound of the fraction of VEGFR-2 molecules in a non-monomeric state (34).

The mobile mode of VEGFR-2 promotes unligated interactions, which in turn enrich the immobile/confined mode

Our observations thus far suggest a relationship between VEGFR-2 mobility and interactions (reflected in the assembly state) in the absence of ligand. To investigate this further, we focused on the dynamic particle merging and splitting events observed in our live-cell imaging streams (Fig. 2A; Movies 4 and 5). These merging and splitting events largely reflected specific

interactions between the imaged molecules, as the dissociation rate for VEGFR-2 interactions calculated from them (34), 0.19-0.26/s, was about one order of magnitude lower than that expected from coincidental overlap due to diffusion (Fig. 2B) (obtained by simulating non-interacting receptors that diffused in 2D in a manner similar to VEGFR-2 and then obtaining the distribution of apparent fusion times caused by resolution limitations (23)).

We found that mobile particles had a higher probability of merging, especially with other mobile particles (Fig. 2C). At the same time, the mobility mode after merging leaned toward imm/conf, for all mode combinations before the merge (Fig. 2D). This was consistent with the observation that imm/conf particles had an overall higher assembly state than mobile particles (Fig. 1D). For particles that stayed mobile after merging, there was some, albeit not always significant, reduction in their diffusion coefficient (Fig. S2). Splitting exhibited the converse relationship, enriching the mobile mode (Fig. 2E and Fig. S2). However, in contrast to the merging probability, which depended on mobility (Fig. 2C), the dissociation rate was the same for both mobility modes (Fig. 2B).

These data provide further support for the presence of dynamic VEGFR-2 interactions (which could be direct or indirect) on the surface of unstimulated HDMECs. The mobile mode of VEGFR-2 promotes these interactions, while they in turn enrich the imm/conf subpopulation, resulting in a complex interplay between VEGFR-2 mobility and interactions.

The dynamics of cell surface VEGFR-2 are reduced upon HDMEC stimulation with VEGF

What role does the dynamic organization of VEGFR-2 play in VEGF-VEGFR-2 binding and signaling? As a first step to address this question, we performed single-molecule imaging of

VEGFR-2 after stimulating HDMECs with 2 nM VEGF (specifically VEGF-A_{165} (4, 7, 32, 35)), which led to robust VEGFR-2 activation that peaked at 5 min (Fig. S3A, B).

Because the effect of VEGF is time-dependent (Fig. S3A, B), and because the 20 s duration of a single-molecule imaging stream were too short to observe potential changes in VEGFR-2 behavior over minutes, we devised a "time-course" imaging and analysis strategy that allowed us to study single-molecule properties on time-scales relevant to cellular processes. In brief, we imaged multiple cells within the course of an experiment (1 cell every 3-4 min, for ~25 min total time), keeping track of their acquisition time relative to the addition of VEGF (usually just before imaging the second cell in a time-course; Fig. 3A). For data analysis ("time-course analysis" or TCA), multiple such time-courses were aligned either by the time point of VEGF addition, or time 0 (i.e. first cell) in the case of unstimulated cells. This allowed us to group cells based on time in order to investigate their single-molecule properties over longer time scales than captured by individual single-molecule imaging streams.

While the two mobility modes of VEGFR-2 were conserved in the presence of VEGF (Fig. 3B), TCA revealed that there was a gradual decrease over time in the probability of the mobile mode, starting at 5-10 min after VEGF addition (Fig. 3C). In contrast to this gradual population shift, D_{mobile} exhibited an almost immediate reduction upon VEGF addition, down to ~0.135 $\mu m^2/s$ (Fig. 3D). $D_{imm/conf}$ did not change (Fig. 3E). The sharp reduction in D_{mobile} upon VEGF exposure was faster than the cellular signaling response to VEGF (Fig. S3), making it unlikely to be due to an overall change in cellular state due to VEGF exposure. Additionally, we did not detect changes in the probability of particle merging based on mobility, or in the mobility mode distribution upon merging (Fig. S3C, D), ruling out the possibility that the drop in D_{mobile} was because of the relationship between VEGFR-2 interactions and mobility. These results suggest that the fast

change in D_{mobile} was due to either conformational changes in VEGFR-2 upon VEGF binding (15), the association of VEGFR-2 with co-receptors (36, 37), leading potentially also to changes in the lipid environment around VEGFR-2, or initial interactions with downstream effectors that precede the full scale signaling response.

Exposure to VEGF also reduced the overall rate of merging between detected VEGFR-2 particles (Fig. 3F). This rate is for all particles regardless of their mobility mode, akin to an overall association rate (but for only the labeled subset of VEGFR-2 molecules). The reduction in merging rate upon VEGF addition is consistent with the reduction in VEGFR-2 mobility (Fig. 3C, D) while keeping the probability of merging per mobility mode pair approximately the same (Fig. S3C). Note that the merging probability increased for imm/conf-imm/conf pairs (Fig. S3C), but this probability is so low compared to the merging probability for pairs that involve a mobile particle that it has little effect on the overall merging rate. These observations strongly suggest that the canonical model of VEGF-induced VEGFR-2 dimerization is not the only pathway of VEGFR-2 activation by VEGF, because in that case we would expect to see an increase, at least transiently, in the rate of VEGFR-2 merging upon VEGF addition.

Co-imaging of VEGFR-2 and VEGF reveals that VEGF binds to and stabilizes non-monomeric states of VEGFR-2

The above experiments and analyses, especially the reduction in VEGFR-2 merging rate upon VEGF addition, suggest that a substantial fraction of VEGF binds to pre-existing VEGFR-2 dimers on the surface of HDMECs, with which it is expected to bind with higher avidity (16, 17). To investigate this question further, we performed simultaneous 2-color TIRFM imaging of VEGFR-2 (labeled as above) and VEGF (conjugated with Atto488, which did not interfere with VEGF

function (Fig. S4)) in order to assess VEGF-VEGFR-2 association at the level of individual VEGFR-2 molecules. To increase the chance of observing colocalization between a labeled VEGFR-2 molecule and a labeled VEGF molecule, we labeled VEGF at a relatively high density (40% of the 2 nM dose was labeled). At this density, we were still able to detect single-particles of VEGF using Gaussian mixture-model fitting (30). However, the density was sometimes too high for reliable tracking of labeled VEGF particles. Therefore, we tracked VEGFR-2 particles as above, and then associated VEGFR-2 tracks in each frame with co-localized VEGF particle detections (38) (Fig. 4A; Movie 6). With this, we analyzed the mobility, assembly state and interactions of VEGFR-2 in the context of its association with VEGF, within the framework of TCA.

Consistent with the global mobility trends observed above (Fig. 3C, D), this analysis revealed that, at the level of individual VEGFR-2 molecules, VEGF association both promoted the switch from mobile to imm/conf (Fig. 4B), and the reduction in D_{mobile} for molecules that stayed mobile while associated with VEGF (Fig. 4C). Interestingly, we found that a larger fraction of imm/conf VEGFR-2 particles were positive for labeled VEGF than mobile VEGFR-2 particles, implying that VEGF had a higher probability to bind to VEGFR-2 in the imm/conf mode (Fig. 4D). We reasoned that this could be because of the overall higher assembly state of imm/conf particles (Fig. 1D).

Indeed, the assembly state of VEGFR-2 particles positive for labeled VEGF was overall higher than that of VEGFR-2 particles negative for labeled VEGF, and it increased over time (Fig. 4E). Of note, because of labeling only 40% of VEGF molecules, some VEGFR-2 particles in the negative group could still be associated with unlabeled VEGF (which would be invisible). This analysis could however not inform us whether VEGF promoted the formation of higher-order

assembly states or whether they existed prior to VEGF association. To reduce this ambiguity, we measured the waiting time from the start of each VEGFR-2 track to its moment of labeled VEGF association. We found a wide range of times until VEGF association for tracks of all assembly states (Fig. 4F), consistent with the notion of pre-existing, unligated VEGFR-2 assemblies on the surface of live endothelial cells.

These experiments also allowed us to investigate the relationship between VEGFR-2 merging and splitting (i.e. dynamic interactions) and VEGF association. Among the interaction events that were positive for labeled VEGF, we found that in half of them the association with VEGF happened before the merge of the two VEGFR-2 particles, while in the other half it happened after the merge of the two VEGFR-2 particles (Fig. 4G). We also observed interaction events negative for labeled VEGF, which allowed us to assess the effect of VEGF association on the stability of VEGFR-2 interactions. We found that the dissociation rate of interaction events positive for labeled VEGF was about half that of interaction events negative for labeled VEGF (Fig. 4H), indicating that association with VEGF stabilizes VEGFR-2 interactions.

Altogether, this analysis provided further evidence that at least a subpopulation of VEGFR-2 on the surface of primary HDMECs exists in higher-order assembly states (dimers, oligomers, clusters or complexes) at rest, which most likely enhance VEGF binding to cells (16, 17). This is however not exclusive, and some VEGF probably binds to VEGFR-2 monomers as well (Fig. 4G). Our data also clearly demonstrate that VEGF stabilizes VEGFR-2 interactions (Fig. 4H). This stabilization most likely underlies the overall increase in VEGFR-2 assembly state upon VEGF addition but with little change in the merging probability of VEGFR-2 (Fig. 4E; Fig. S3C).

VEGFR-2 phosphorylation promotes the imm/conf mode of VEGFR-2

VEGF-VEGFR-2 binding leads to tyrosine phosphorylation of the intracellular domain of VEGFR-2 (Fig. S3). Thus, the observed effects of VEGF on VEGFR-2 behavior could be because of VEGF binding itself or because of VEGFR-2 phosphorylation and downstream events. To distinguish between these two scenarios, we performed single-molecule imaging followed by TCA for HDMECs in the presence of the VEGFR phosphorylation inhibitor AAL-993 (39), using a 30 nM dose for 1 h, which largely abolished VEGFR-2 activation by VEGF (Fig. S3A-B). These experiments also allowed us to investigate the role of VEGFR-2 phosphorylation in unstimulated cells, as previous studies have provided evidence for VEGFR-2 phosphorylation resulting from unligated dimerization (15). While weak, we did in fact observe a slight reduction in VEGFR-2 phosphorylation in the presence of AAL-993 in unstimulated cells (Fig. S3B).

Diffusion analysis and TCA revealed that the two mobility modes of VEGFR-2 were conserved also in the presence of AAL-993, but now with a shift toward the mobile mode (i.e. opposite of the effect of VEGF), both in unstimulated and VEGF-stimulated cells (Fig. 5A-C). Parallel to the increase in mobile VEGFR-2 particles, there was also an increase in the merging rate of VEGFR-2, both in the absence and presence of VEGF (Fig. S5A, B). Otherwise, AAL-993 seemed to have little effect on the merging probability of VEGFR-2 based on mobility, or the dissociation rate of its interactions (Fig. S5C, D). Interestingly, in contrast to the shift in modes from imm/conf to mobile, the almost immediate reduction of the diffusion coefficient of mobile VEGFR-2 particles (D_{mobile}) upon VEGF stimulation was insensitive to the presence of AAL-993 (Fig. 5D).

These observations suggest that VEGFR-2 phosphorylation upon VEGF binding plays a role in the shift in mobility mode from mobile to imm/conf, but that the change in D_{mobile} upon VEGF binding is upstream of VEGFR-2 phosphorylation. Our observation that phosphorylation

inhibition by AAL-993 promotes the mobile mode even in unstimulated cells suggests that phosphorylation and interactions (even if transient) with intracellular partners play a role in regulating VEGFR-2 mobility even in the absence of ligand.

Discussion

To the best of our knowledge, this study is the first single-molecule study of VEGFR-2 in its native plasma membrane environment in primary HDMECs, exposing its previously unknown dynamic nanoscale organization on the EC surface. We found that cell surface VEGFR-2 molecules can be mobile or imm/conf, both of which can be monomeric or non-monomeric, even in unstimulated cells (Fig. S6A-C). The mobile mode promotes VEGFR-2 encounters and interactions, which in turn enrich the imm/conf mode. The relationship however is not one-to-one: Many molecules remain mobile after interacting with each other, and, conversely, some imm/conf molecules appear to be monomeric. While the tendency for interactions depends on mobility mode, the dissociation rate of the non-monomeric state is similar between the two modes.

Phosphorylation inhibition experiments suggest that the imm/conf mode depends on VEGFR-2 phosphorylation, even in unstimulated cells, where it could be due to unligated dimerization (15) or association with Src family kinases (18-20). Thus the imm/conf mode is at least partially due to interactions with downstream effectors and scaffolds (6, 32, 33). Further studies are needed to investigate the role that these factors, as well as other ubiquitous factors such as the cytoskeleton or membrane nano/micro-domains (23, 40-43), play in regulating VEGFR-2 mobility on the EC surface.

Our observation that VEGFR-2 can be non-monomeric in its native plasma membrane environment in unstimulated HDMECs, with the full slew of native regulatory factors, corroborates previous reports of unligated dimerization of exogenously expressed VEGFR-2 in non-endothelial cells and in vesicles derived from their plasma membranes (15, 44). With this, VEGFR-2 joins the ranks of many other RTK's for which there is growing evidence of unligated dimerization (10-14). Regarding VEGFR-2 activation by VEGF, our data suggest that both the

canonical model of ligand-induced dimerization and the alternative model of ligand binding to pre-existing dimers co-exist (Fig. S6D-F). Evidence for the canonical model comes from the observation that the probability of imm/conf VEGFR-2 merging increases in the presence of VEGF and that in half of the observed merging events VEGFR-2 associates with VEGF before the merge. Evidence for the alternative model comes from the observation that in the other half of merging events VEGFR-2 associates with VEGF only after the merge, that higher-order assembly states exist before VEGF association, and that the overall rate of merging decreases after VEGF addition. The steady decrease in merging rate suggests that the alternative model is most likely dominant.

Our experiments also revealed the effect of VEGF on VEGFR-2 behavior. In addition to the expected increase in imm/conf VEGFR-2 because of activation and interactions with scaffolds and downstream effectors, our experiments also revealed an almost immediate drop in VEGFR-2 diffusion coefficient for the molecules that stay mobile upon VEGF binding. This drop is independent of phosphorylation, suggesting that it is due to either conformational changes in VEGFR-2 upon VEGF binding (15) or the association of VEGFR-2 with co-receptors through VEGF (36, 37), leading potentially also to changes in the lipid environment around VEGFR-2. VEGF also stabilizes VEGFR-2 interactions, leading to an about 2-fold reduction in their dissociation rate. This contributes to the increase in VEGFR-2 non-monomeric states upon VEGF addition without an associated increase in VEGFR-2 dimerization.

Our study reveals the dynamic nanoscale organization of VEGFR-2 in its native environment on the surface of HDMECs, shedding light on the cell biophysical properties of this developmentally important receptor. In light of the higher avidity of VEGF to dimeric VEGFR-2 (16, 17), this nanoscale organization most likely plays an important role in the responsiveness of ECs to VEGF. This nanoscale organization might also play a role in the responsiveness of ECs to

shear stress (18-20). Thus determining the mechanisms that regulate the cell surface organization of VEGFR-2 and linking them to VEGFR-2 signaling will be central for our understanding of endothelial cell behavior and function in development and disease.

Materials and methods

Detailed materials and methods, experimental and computational, are described in the Supporting Information (SI) Appendix. Briefly, all experiments employed early-passage primary HDMECs isolated from neonatal foreskin. For VEGFR-2 imaging, anti-VEGFR-2 Fab fragments were generated from the monoclonal antibody EIC using ficin digestion. For VEGF imaging, VEGF was conjugated with Atto488 through the succinimidyl ester group of the dye. After labeling, cells were imaged at 37°C using a TIRF microscope with one-color or simultaneous two-color imaging modalities. The imaged molecules were then detected and tracked using u-track (30), followed by diffusion mode analysis (31) and assembly state and dissociation rate analysis (34). For VEGF and VEGFR-2 co-imaging experiments, VEGF-VEGFR-2 association was determined by solving a linear assignment problem with a 4-pixel distance cutoff (45), followed by temporal stability criteria. For time course analysis, two strategies were followed: (1) Single-molecule properties were calculated per cell and then individual cell measurements were grouped by time interval. (2) For properties with too few data points per cell, leading to noisy individual cell measurements, the tracks within the cell group of interest were combined, and then the single-molecule properties were calculated from the combined tracks. The various statistical tests used for data comparison between conditions or time intervals are stated in the figure legends and explained in detail in the SI Appendix.

Acknowledgments

We thank Dr. Tieqiao (Tim) Zhang for microscopy support, Dr. Ashley Lakoduk for sharing molecular biology expertise, and Dr. Luke Rice for feedback on the manuscript. This work was supported by funding from NIH/NIGMS (R35 GM119619), The Welch Foundation (I-1901), CPRIT (R1216) and the UT Southwestern Endowed Scholars Program to KJ.

Author contributions

B.R.A. and K.J. designed research; B.R.A., S.L. and A.D. performed experiments; A.R.V., L.R.O., T.K., M.K. and K.J. wrote analysis software; B.R.A. and K.J. performed analysis; B.R.A. and K.J. wrote the paper with input from all co-authors.

Figure legends

Figure 1. Single-molecule imaging exposes motion and organization heterogeneity of VEGFR-2 on the surface of unstimulated HDMECs. (A) Representative TIRF microscopy image of RRX-labeled VEGFR-2 in unstimulated HDMEC. Scale bar, 5 μm. Image inverted for visual clarity. **(B)**. VEGFR-2 diffusion coefficient distribution under unstimulated conditions. Vertical dashed line: threshold separating the two mobility modes. **(C)** VEGFR-2 tracks over a 10 Hz/20 s imaging stream, colored based on mobility mode (red = mobile, blue = imm/conf, and black = too short to classify (duration < 5 frames)). Same cell and area as in (A). **(D)** Normalized frequency of apparent assembly state of detected VEGFR-2 particles in the two mobility modes and in a sample with highly diluted labeling, the latter reflecting the number of fluorophores per secondary Fab fragment. Error bars: standard deviations from 100 bootstrap samples. Asterisks: p-value < 10^{-15} when comparing corresponding frequencies between the indicated conditions

(assuming normal distributions with standard deviations obtained by bootstrapping); ns (not significant): p-value > 0.05. N: VEGFR-2: 140,445 tracks (53,417 with duration ≥ 5 frames) from 9 independent experiments with 9-11 cells each; Highly diluted sample: 8751 tracks (2,200 with duration ≥ 5 frames) from 2 independent experiments with 10 cells each.

Figure 2. VEGFR-2 mobility and interactions in unstimulated HDMECs exhibit a complex relationship. (A) Series of images showing an event of VEGFR-2 particle merging and splitting in an unstimulated cell. Scale bar (applicable to all sub-panels), 1 μm. Images inverted for visual clarity. **(B)** Dissociation rates of VEGFR-2 per mobility mode as observed experimentally in unstimulated HDMECs (experiments) and from simulations of coincidental overlap within the resolution limit (simulations; described in Materials and Methods). Red and blue filled circles (also in C-E) represent mobile and imm/conf particles, respectively. **(C)** Probability of VEGFR-2 merging in unstimulated cells per combination of mobility modes. **(D)** Probability of mobility mode for merged particle based on the combination of particle mobility modes before merging. Red and blue bars (also in (E)) indicate mobile and imm/conf modes, respectively. **(E)** Probability of mobility mode combination for particles after splitting based on the mobility mode of the spitting particle. Purple bars indicate the probability of producing one mobile and one imm/conf particle. Error bars in (B-E): standard deviation from 100 bootstrap samples. Asterisks in (B-C): p-value < 10^{-10} when comparing between the indicated conditions (assuming normal distributions with standard deviations obtained by bootstrapping); ns (not significant): p-value > 0.05. In (D-E), ns (i.e. p-value > 0.05) indicates the probability is not significantly different from 0 (assuming normal distributions with standard deviations obtained by bootstrapping). N same as in Fig. 1.

Figure 3. Time-course analysis reveals reduction in cell surface VEGFR-2 mobility and merging rate upon HDMEC stimulation with VEGF. (A) Cartoon illustrating time-course imaging. **(B)** VEGFR-2 diffusion coefficient distribution on the surface of unstimulated (black) and 2nM VEGF-stimulated (magenta) HDMECs. Unstimulated distribution and vertical dashed line are a repeat of Fig. 1B. **(C-F)** Time-courses of the probability of VEGFR-2 molecules belonging to the mobile mode **(C)**, the mean diffusion coefficient of mobile molecules **(D)** and imm/conf molecules **(E)** (note the different y-axis ranges in (D) and (E)), and the rate of merging **(F)**. Black and magenta: measurements from unstimulated and VEGF-stimulated time-courses, respectively. Vertical magenta line: mean time point of VEGF addition (thus measurements at times before the vertical magenta line are from unstimulated cells, even in the stimulated time-course). Dots: individual cell values. Lines and surrounding shaded areas: the mean and standard error of the mean, respectively, from cells grouped into 5-min intervals as indicated. Asterisks above time intervals: p-value < 0.05 for comparing stimulated and unstimulated measurements per time interval using a t-test. Time intervals without an asterisk: no significant difference between stimulated and unstimulated measurements (p-value > 0.05). N: Unstimulated: same as in Fig. 1; Stimulated: 99,699 (42,865 with duration ≥ 5 frames) from 8 independent experiments with 9-10 cells each.

Figure 4. Co-imaging of VEGFR-2 and VEGF allows dissection of the relationship between individual VEGFR-2 molecules associating with VEGF and their mobility and interactions . (A) A track of RRX-labeled VEGFR-2 (magenta) and its associated Atto488-labeled VEGF (light green), overlaid on the merged image of the 561 (magenta) and 488 (green) channels in the last displayed frame (at 9.4 s). Scale bar, 500 nm. **(B)** Time-course of fraction of VEGFR-2 tracks in

the imm/conf mode while associated with an Atto488-VEGF particle, per mobility mode before VEGF association. Lines and surrounding shaded areas: measured parameter and its standard deviation from 100 bootstrap samples. **(C)** Time course of the diffusion coefficient, before and during VEGF association, of VEGFR-2 particles that are mobile both before and during VEGF association. Lines and surrounding shaded areas as in (B). Asterisks above time intervals: p-value $< 10^{-5}$ for comparing the two measurements in each time interval (assuming normal distributions with standard deviations from bootstrapping). **(D)** Time course of fraction of VEGFR-2 tracks getting associated with Atto488-VEGF per VEGFR-2 mobility mode. Lines and surrounding shaded areas as in (B). Asterisks as in (C). **(E)** Normalized frequency of apparent assembly state of detected VEGFR-2 particles associated (VEGF positive) or not (VEGF negative) with Atto488-VEGF, in the indicated time intervals. Error bars: standard deviations from 100 bootstrap samples. Asterisks and ns: p-value < 0.005 and p-value > 0.05, respectively, when comparing corresponding frequencies between the indicated conditions (assuming normal distributions with standard deviations obtained by bootstrapping). **(F)** Normalized frequency of waiting times between the start of a VEGFR-2 track and its association with Atto488-VEGF, for the subset of tracks that associate with VEGF after their first time point (23% of $n = 1$ tracks and 60% of $n > 1$ tracks). **(G)** Time-course of fraction of merging events where VEGFR-2 association with Atto488-VEGF occurs before the merge. Lines and surrounding shaded areas as in (B). **(H)** Dissociation rates of VEGFR-2 undergoing interactions associated (+) or not (-) with Atto488-VEGF, for $n = 2$ or $n = 3$ assembly states. Error bars as in (E). N: 189,097 tracks (81188 with duration ≥ 5 frames) from 10 independent experiments with 8-10 cells each.

Figure 5. The probabilities of the two mobility modes of VEGFR-2, but not D_{mobile}, depend on VEGFR-2 phosphorylation. (A) VEGFR-2 diffusion coefficient distribution on the surface of HDMECs: unstimulated (black), stimulated with 2 nM VEGF (magenta), unstimulated in the presence of 30 nM AAL-993 (orange), and VEGF-stimulated in the presence of AAL-993 (green). Unstimulated and VEGF-stimulated (both in the absence of AAL-993) distributions and vertical dashed line are a repeat of Fig. 3B. **(B-D)** Time-courses of the probability of VEGFR-2 molecules belonging to the mobile mode in unstimulated cells in the absence or presence of AAL-993 **(B)** and in VEGF-stimulated cells in the absence or presence of AAL-993 **(C)**, and the mean diffusion coefficient of mobile molecules in all conditions **(D)**. Dots, lines and surrounding shaded areas, and vertical magenta line as in Fig. 3C-F. Asterisks in (B-C): p-value < 0.02 for comparing the total time course between conditions using a paired t-test (in (C) the comparison is only for the time intervals after VEGF addition). Asterisks above time intervals in (D): p-value < 0.05 for comparing the measurements with and without VEGF stimulation in the presence of AAL per time interval using a t-test. N: Unstimulated: same as in Fig. 1; + VEGF: Same as in Fig. 3; unstimulated AAL: 133,815 tracks (48,851 with duration ≥ 5 frames) from 8 independent experiments with 9-11 cells each; AAL + VEGF: 134,371 tracks (54,198 with duration ≥ 5 frames) from 9 independent experiments with 9-10 cells each.

References

1. Chung AS & Ferrara N (2011) Developmental and pathological angiogenesis. *Annu Rev Cell Dev Biol* 27:563-584.
2. Carmeliet P & Jain RK (2011) Molecular mechanisms and clinical applications of angiogenesis. *Nature* 473(7347):298-307.
3. Apte RS, Chen DS, & Ferrara N (2019) VEGF in Signaling and Disease: Beyond Discovery and Development. *Cell* 176(6):1248-1264.
4. Ferrara N, Gerber HP, & LeCouter J (2003) The biology of VEGF and its receptors. *Nat Med* 9(6):669-676.

5. Terman BI*, et al.* (1992) Identification of the KDR tyrosine kinase as a receptor for vascular endothelial cell growth factor. *Biochem Biophys Res Commun* 187(3):1579-1586.
6. Olsson AK, Dimberg A, Kreuger J, & Claesson-Welsh L (2006) VEGF receptor signalling - in control of vascular function. *Nat. Rev. Mol. Cell Biol.* 7(5):359-371.
7. Simons M, Gordon E, & Claesson-Welsh L (2016) Mechanisms and regulation of endothelial VEGF receptor signalling. *Nat Rev Mol Cell Biol* 17(10):611-625.
8. Karaman S, Leppanen VM, & Alitalo K (2018) Vascular endothelial growth factor signaling in development and disease. *Development* 145(14):8.
9. Ruch C, Skiniotis G, Steinmetz MO, Walz T, & Ballmer-Hofer K (2007) Structure of a VEGF–VEGF receptor complex determined by electron microscopy. *Nature Structural &Amp; Molecular Biology* 14:249.
10. Chung I*, et al.* (2010) Spatial control of EGF receptor activation by reversible dimerization on living cells. *Nature* 464(7289):783-787.
11. Lin C-C*, et al.* (2012) Inhibition of Basal FGF Receptor Signaling by Dimeric Grb2. *Cell* 149(7):1514-1524.
12. Low-Nam ST*, et al.* (2011) ErbB1 dimerization is promoted by domain co-confinement and stabilized by ligand binding. *Nat Struct Mol Biol* 18(11):1244-1249.
13. Mischel PS*, et al.* (2002) Nerve Growth Factor Signals via Preexisting TrkA Receptor Oligomers. *Biophysical Journal* 83(2):968-976.
14. Bogdanovic E, Coombs N, & Dumont DJ (2009) Oligomerized Tie2 localizes to clathrin-coated pits in response to angiopoietin-1. *Histochem. Cell Biol.* 132(2):225-237.
15. Sarabipour S, Ballmer-Hofer K, & Hristova K (2016) VEGFR-2 conformational switch in response to ligand binding. *Elife* 5:e13876.
16. Fuh G, Li B, Crowley C, Cunningham B, & Wells JA (1998) Requirements for binding and signaling of the kinase domain receptor for vascular endothelial growth factor. *J Biol Chem* 273(18):11197-11204.
17. King C & Hristova K (2019) Direct measurements of VEGF-VEGFR2 binding affinities reveal the coupling between ligand binding and receptor dimerization. *J Biol Chem* 294(23):9064-9075.
18. Chen KD*, et al.* (1999) Mechanotransduction in response to shear stress - Roles of receptor tyrosine kinases, integrins, and Shc. *J. Biol. Chem.* 274(26):18393-18400.
19. Jin ZG*, et al.* (2003) Ligand-independent activation of vascular endothelial growth factor receptor 2 by fluid shear stress regulates activation of endothelial nitric oxide synthase. *Circ Res* 93(4):354-363.
20. Tzima E*, et al.* (2005) A mechanosensory complex that mediates the endothelial cell response to fluid shear stress. *Nature* 437(7057):426-431.
21. Lemmon MA & Schlessinger J (2010) Cell Signaling by Receptor Tyrosine Kinases. *Cell* 141(7):1117-1134.
22. Githaka JM*, et al.* (2016) Ligand-induced growth and compaction of CD36 nanoclusters enriched in Fyn induces Fyn signaling. *J Cell Sci* 129(22):4175-4189.
23. Jaqaman K*, et al.* (2011) Cytoskeletal control of CD36 diffusion promotes its receptor and signaling function. *Cell* 146(4):593-606.
24. Treanor B*, et al.* (2010) The Membrane Skeleton Controls Diffusion Dynamics and Signaling through the B Cell Receptor. *Immunity* 32(2):187-199.
25. Zhou Y*, et al.* (2017) Lipid-Sorting Specificity Encoded in K-Ras Membrane Anchor Regulates Signal Output. *Cell* 168(1-2):239-+.
26. Casaletto JB & McClatchey AI (2012) Spatial regulation of receptor tyrosine kinases in development and cancer. *Nat. Rev. Cancer* 12(6):386-399.

27. Garcia-Parajo MF, Cambi A, Torreno-Pina JA, Thompson N, & Jacobson K (2014) Nanoclustering as a dominant feature of plasma membrane organization. *J. Cell Sci.* 127(23):4995-5005.
28. Liu Z, Lavis LD, & Betzig E (2015) Imaging live-cell dynamics and structure at the single-molecule level. *Mol Cell* 58(4):644-659.
29. Xia T, Li N, & Fang X (2013) Single-molecule fluorescence imaging in living cells. *Annu Rev Phys Chem* 64:459-480.
30. Jaqaman K*, et al.* (2008) Robust single-particle tracking in live-cell time-lapse sequences. *Nat Methods* 5(8):695-702.
31. Jaqaman K, Galbraith JA, Davidson MW, & Galbraith CG (2016) Changes in single-molecule integrin dynamics linked to local cellular behavior. *Mol Biol Cell* 27(10):1561-1569.
32. Lampugnani MG, Orsenigo F, Gagliani MC, Tacchetti C, & Dejana E (2006) Vascular endothelial cadherin controls VEGFR-2 internalization and signaling from intracellular compartments. *J Cell Biol* 174(4):593-604.
33. Labrecque L*, et al.* (2003) Regulation of vascular endothelial growth factor receptor-2 activity by caveolin-1 and plasma membrane cholesterol. *Mol Biol Cell* 14(1):334-347.
34. De Oliveira LR & Jaqaman K (2019) FISIK: Framework for the Inference of In Situ Interaction Kinetics from Single-Molecule Imaging Data. *Biophys J* 117(6):1012-1028.
35. Hamdollah Zadeh MA, Glass CA, Magnussen A, Hancox JC, & Bates DO (2008) VEGF-mediated elevated intracellular calcium and angiogenesis in human microvascular endothelial cells in vitro are inhibited by dominant negative TRPC6. *Microcirculation (New York, N.Y. : 1994)* 15(7):605-614.
36. Gelfand MV*, et al.* (2014) Neuropilin-1 functions as a VEGFR2 co-receptor to guide developmental angiogenesis independent of ligand binding. *Elife* 3:e03720.
37. Somanath PR, Malinin NL, & Byzova TV (2009) Cooperation between integrin alphavbeta3 and VEGFR2 in angiogenesis. *Angiogenesis* 12(2):177-185.
38. Loerke D, Mettlen M, Schmid SL, & Danuser G (2011) Measuring the hierarchy of molecular events during clathrin-mediated endocytosis. *Traffic* 12(7):815-825.
39. Manley PW*, et al.* (2002) Anthranilic acid amides: a novel class of antiangiogenic VEGF receptor kinase inhibitors. *J Med Chem* 45(26):5687-5693.
40. Andrews NL*, et al.* (2008) Actin restricts Fc epsilon RI diffusion and facilitates antigen-induced receptor immobilization. *Nat. Cell Biol.* 10(8):955-963.
41. Mattila PK*, et al.* (2013) The Actin and Tetraspanin Networks Organize Receptor Nanoclusters to Regulate B Cell Receptor-Mediated Signaling. *Immunity* 38(3):461-474.
42. Jaqaman K & Grinstein S (2012) Regulation from within: the cytoskeleton in transmembrane signaling. *Trends Cell Biol.* 22(10):515-526.
43. Sezgin E, Levental I, Mayor S, & Eggeling C (2017) The mystery of membrane organization: composition, regulation and roles of lipid rafts. *Nat. Rev. Mol. Cell Biol.* 18(6):361-374.
44. Warren CM, Ziyad S, Briot A, Der A, & Iruela-Arispe ML (2014) A ligand-independent VEGFR2 signaling pathway limits angiogenic responses in diabetes. *Sci Signal* 7(307):ra1.
45. Jonker R & Volgenant A (1987) A Shortest Augmenting Path Algorithm for Dense and Sparse Linear Assignment Problems. *Computing* 38(4):325-340.

Figure 1

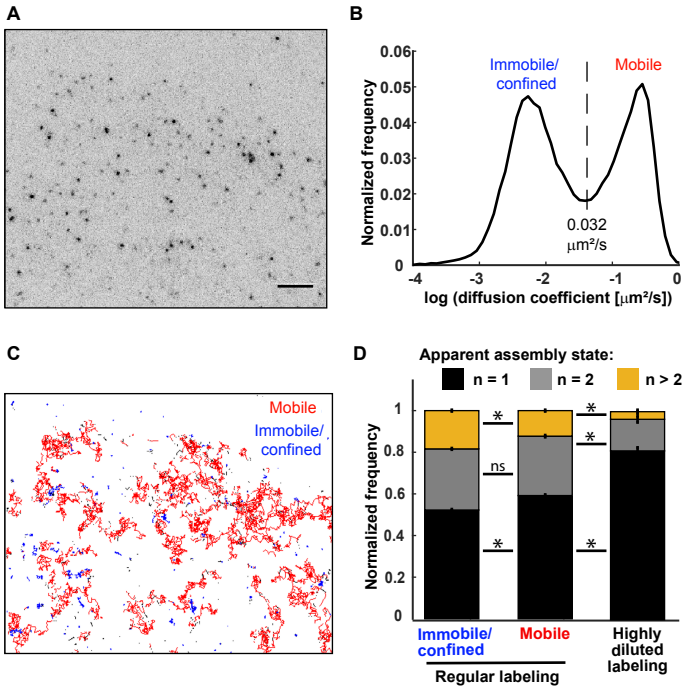
A
B
Immobile/
confined
Mobile
Normalized frequency
0.06
0.05
0.04
0.03
0.02
0.01
0
0.032
μm²/s
-4
-3
-2
-1
0
log (diffusion coefficient [μm²/s])
C
Mobile
Immobile/
confined
D
Apparent assembly state:
n = 1
n = 2
n > 2
Normalized frequency
1
0.8
0.6
0.4
0.2
0
*
ns
*
*
*
Immobile/
confined
Mobile
Highly
diluted
labeling
Regular labeling

Figure 2

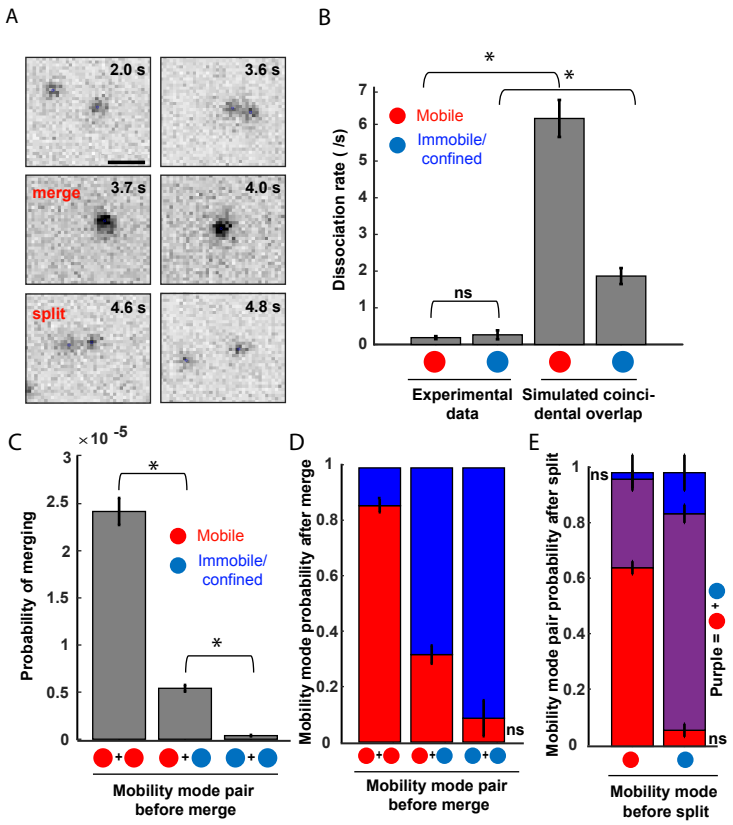
A
2.0 s
3.6 s
merge
3.7 s
4.0 s
split
4.6 s
4.8 s
B
Dissociation rate (/s)
Mobile
Immobile/ confined
ns
*
*
Experimental data
Simulated coincidental overlap
C
×10 -5
Probability of merging
Mobile
Immobile/ confined
*
*
Mobility mode pair before merge
D
Mobility mode probability after merge
ns
Mobility mode pair before merge
E
Mobility mode pair probability after split
ns
ns
Purple = +
Mobility mode before split

Figure 3

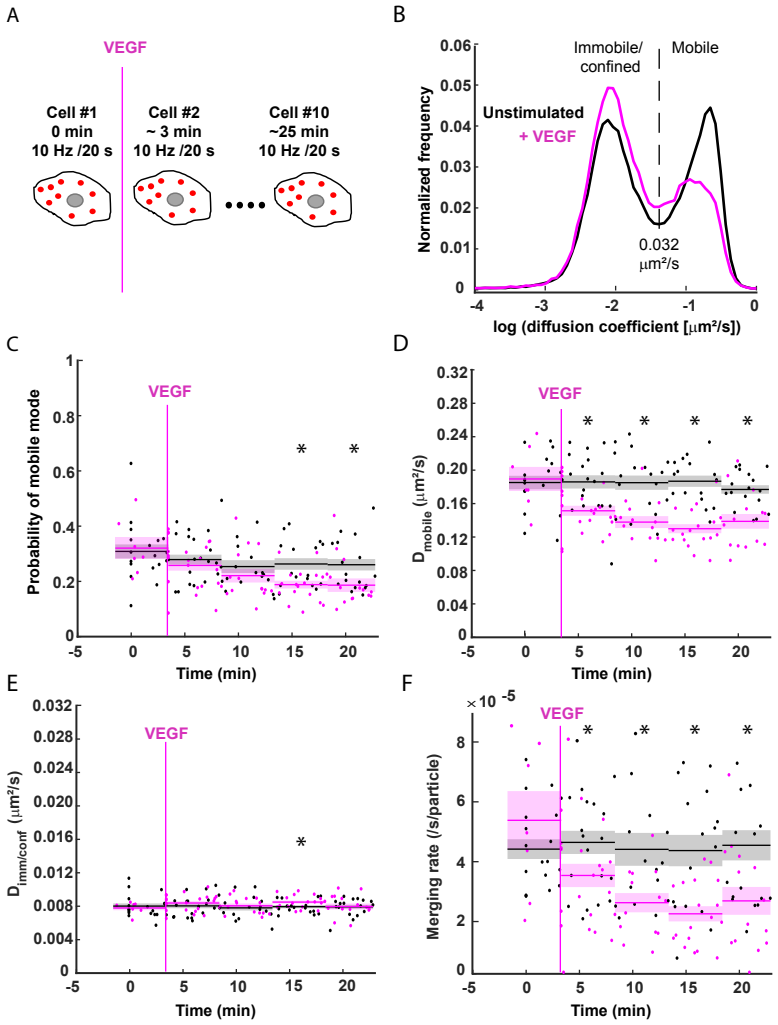
A
VEGF
Cell #1
0 min
10 Hz /20 s
Cell #2
~ 3 min
10 Hz /20 s
Cell #10
~25 min
10 Hz /20 s
B
Immobile/
confined
Mobile
Unstimulated
+ VEGF
0.032
μm²/s
Normalized frequency
log (diffusion coefficient [μm²/s])
C
VEGF
Probability of mobile mode
Time (min)
D
VEGF
D_mobile (μm²/s)
Time (min)
E
VEGF
D_imm/conf (μm²/s)
Time (min)
F
VEGF
×10 -5
Merging rate (/s/particle)
Time (min)

Figure 4

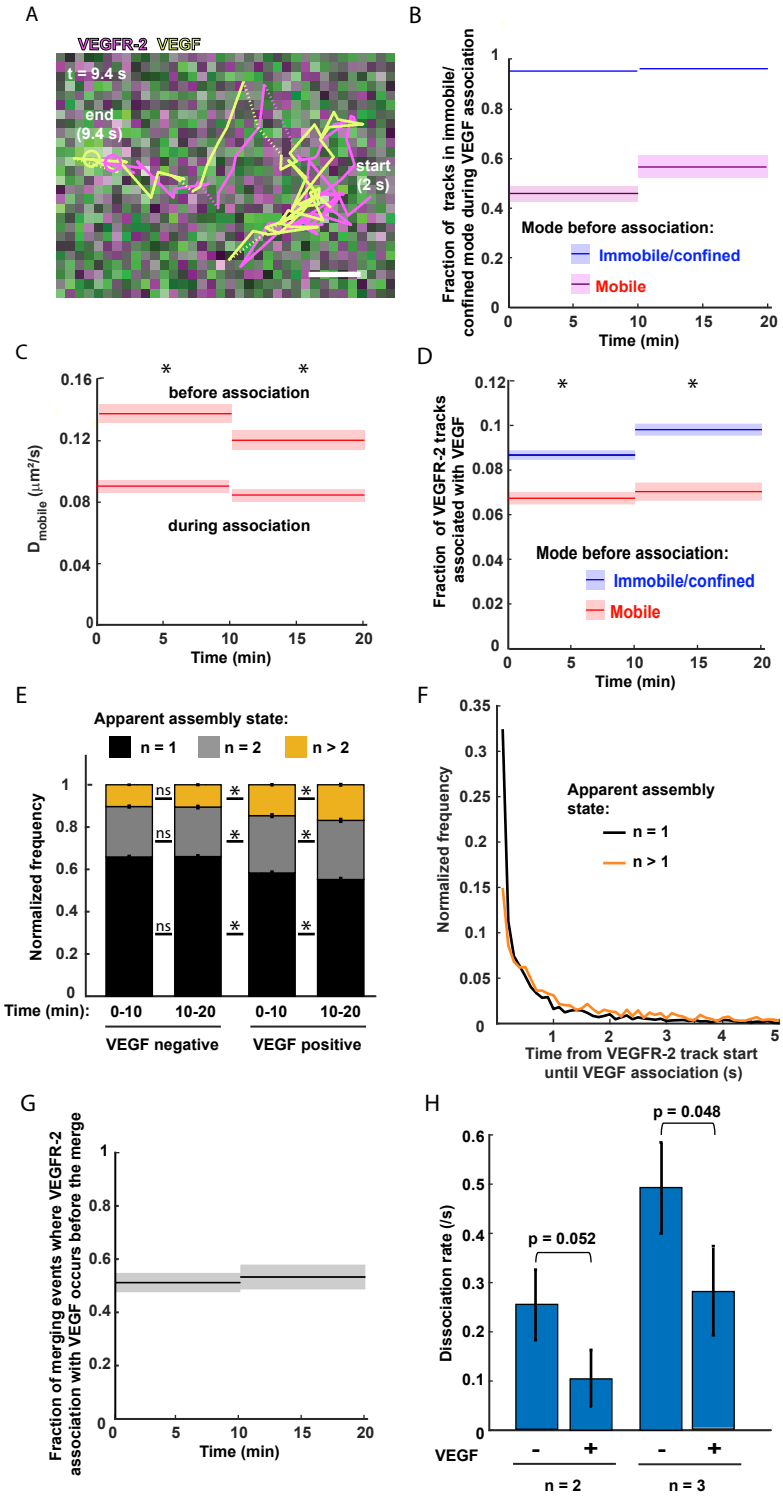
A
VEGFR-2 VEGF
t = 9.4 s
end
(9.4 s)
start
(2 s)
B
Fraction of tracks in immobile/ confined mode during VEGF association
Mode before association:
Immobile/confined
Mobile
Time (min)
C
before association
during association
D_{mobile} (μm²/s)
Time (min)
D
Fraction of VEGFR-2 tracks associated with VEGF
Mode before association:
Immobile/confined
Mobile
Time (min)
E
Apparent assembly state:
n = 1
n = 2
n > 2
Normalized frequency
Time (min):
0-10
10-20
0-10
10-20
VEGF negative
VEGF positive
F
Normalized frequency
Apparent assembly state:
n = 1
n > 1
Time from VEGFR-2 track start until VEGF association (s)
G
Fraction of merging events where VEGFR-2 association with VEGF occurs before the merge
Time (min)
H
p = 0.052
p = 0.048
Dissociation rate (/s)
VEGF
n = 2
n = 3

Figure 5

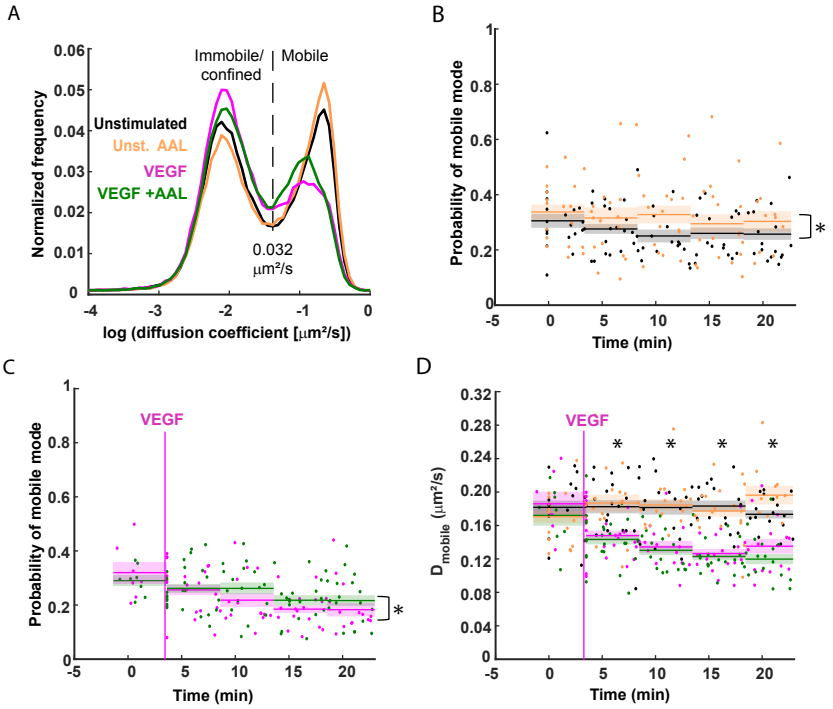
A
Immobile/ confined
Mobile
Unstimulated
Unst. AAL
VEGF
VEGF +AAL
0.032 μm²/s
Normalized frequency
log (diffusion coefficient [μm²/s])
B
Probability of mobile mode
Time (min)
C
VEGF
Probability of mobile mode
Time (min)
D
VEGF
D_mobile (μm²/s)
Time (min)

Supporting Information Appendix

Single-molecule study of the dynamic organization of Vascular Endothelial Growth Factor Receptor 2 on the endothelial cell surface

Bruno da Rocha-Azevedo, Sungsoo Lee, Aparajita Dasgupta, Anthony R. Vega, Luciana R. de Oliveira, Tae Kim, Mark Kittisopikul and Khuloud Jaqaman

Experimental materials and methods

Cell culture and plating. Early passage (P4-P7) primary cultures of human dermal microvascular endothelial cells isolated from neonatal foreskin (HDMECn, LifeLine Cell Technology, Frederick, MD) were grown in VascuLife VEGF-Mv culture medium for 48 h at 37°C + 5% CO2 until reaching 90% confluency. For stimulation, cells were treated with 2 nM VEGFA-165 (Genscript, Piscataway, NJ) at time points indicated in time-course analysis or Western Blots. To inhibit VEGFR-2 phosphorylation, cells were incubated with 30 nM of AAL-993 (MilliporeSigma, Burlington, MA), starting 1h before the experiments and continuing for the duration of the experiments. For single molecule imaging experiments using TIRFM, 5.4 x 10^4 cells were plated 18 h prior to imaging on base/acid cleaned glass bottom dishes (14 mm glass diameter with glass thickness of 1.5 mm, MatTek, Ashland, MA) pre-coated for 45 minutes with 10 µg/ml fibronectin (MilliporeSigma).

Preparation of anti-VEGFR-2 EIC-Fab fragments and fluorescence labeling of VEGF. The Pierce Mouse IgG1 Fab and F(ab')2 Preparation Kit (Thermo Scientific, Waltham, MA) was used to generate Fab fragments from the anti-human VEGFR-2 mouse monoclonal antibody EIC (Abcam, Cambridge, MA). To reach optimal generation of EIC-Fab fragments, 500 µg of antibody were digested with immobilized ficin for 3h at 37°C, and, after the purification steps, the product was concentrated in a 10 kDa cut-off column. VEGF was conjugated with Atto488 through the succinimidyl ester group of the dye, using the Atto protein labeling kit following the manufacturer's directions (MilliporeSigma). The dye-to-protein ratio obtained from the labeled VEGF was 0.4, as determined by spectrophotometry.

VEGFR-2 single molecule labeling. Plated cells were washed once with wash buffer (HBSS + 1 mM HEPES and 0.1% NGS), blocked for 15 min at 37°C in blocking buffer (1% BSA, 5% NGS in wash buffer) and incubated for 15 min with 0.2 µg/ml of primary anti-VEGFR-2 EIC-Fab fragments at 15°C. After 3 washes (1 min, RT), dishes were incubated for 15 min at RT in the dark with 2 µg/ml of a Rhodamine-Red-X (RRX)- conjugated goat anti-mouse secondary Fab fragment (Jackson ImmunoResearch, West Grove, PA). After 3 washes (1 min, RT), dishes were incubated with imaging buffer at 37°C (containing Oxyfluor 1%, Glucose 0.45%, Trolox 2nM) in order to reduce photobleaching. The purpose of the initial incubation with primary Fab fragments at 15°C, then incubation with secondary Fab fragments at RT, and then finally incubation with imaging buffer at 37°C was to minimize receptor and Fab fragment internalization during the labeling period while gently bringing the cells back to 37°C for imaging. VEGF or Atto488-VEGF to be added to cells were diluted in imaging buffer to a final concentration of 2 nM.

To determine the number of fluorophores per secondary fab fragment, the labeling procedure described above was followed, but with a much reduced concentration of primary EIC-Fab fragments (0.1 µg/ml) and of secondary Fab fragments (0.045 µg/ml).

Live-cell single-molecule imaging. Cells were imaged at 37°C using an S-TIRF system (Spectral Applied Research, via BioVision Technologies, Exton, PA) mounted on a Nikon Ti-E inverted microscope with Perfect Focus and a 60x/1.49 NA oil TIRF objective (Nikon Instruments, Melville, NY). The system was equipped with two Evolve EMCCD cameras (Photometrics, Tucson, AZ) for one-color or simultaneous two-color imaging, registered to within 1-3 pixels of each other. A custom 3x tube lens was employed to achieve an 89 nm pixel size in the recorded image. Illumination by a 561 nm diode pumped solid state laser (Cobolt) and/or a 488 nm diode laser (Coherent) was achieved through an ILE laser merge module (Spectral Applied Research), with 488 nm and 561 nm laser power of 3.65 mW and 13.2 mW, respectively, at the coverslip. The penetration depth was set to 80 nm via the Diskovery platform control (Spectral Applied Research). Videos were acquired with MetaMorph (Molecular Devices, San Jose, CA) in stream mode at 100 ms per frame (i.e. 10 Hz sampling) for 200 frames, using an EM gain of 100. Temperature and humidity were maintained using an environment chamber (Okolab, Otaviano, Italy), maintaining cell viability for the duration of the experiments. Every single-molecule imaging stream Is preceded by a brightfield snapshot of the imaged cell region in order to delineate the cell mask (manually) for any ensuing analysis.

Western Blotting. After cell treatment (or not) with VEGF, Atto488-VEGF, and/or AAL-993 for the indicated times, cells were treated with lysis buffer (Mammalian-PE LB Buffer, GoldBio, St.

Louis, MO) and a protease/phosphatase inhibitor cocktail (Thermo Scientific) for 10 min on ice under agitation. Lysates were collected after centrifugation, re-suspended in Laemmli sample buffer, and heated (90°C for 10 min). Samples were loaded in 4-15% gradient SDS-PAGE Mini-PROTEAN TGX gels (Bio-Rad, Hercules, CA). Proteins were transferred to PVDF membranes (100 V / 1h / 4°C) and blocked using 5% BSA in TBST. Rabbit anti-human antibodies against VEGFR-2 (55B11, 1/2000 dilution, Cell Signaling, Danvers, MA), Y1175 phospho-VEGFR-2 (19A10, 1/1000 dilution, Cell Signaling), actin (1/1000 dilution, MilliporeSigma) and/or GAPDH (1/2500 dilution, Abcam) were incubated with membranes for 18h at 4°C. Goat anti-Rabbit secondary antibody conjugated with HRP (1/5000 dilution, Thermo Scientific) was incubated for 1 h at RT in the dark. Protein bands were detected by chemiluminescence using Clarity Western ECL Substrate (BioRad), and densitometric analyses were made using Image Lab (BioRad).

Computational image and data analysis

Computing environment. All image and data analysis tasks were performed in Matlab 2017a and more recent versions (The MathWorks, Natick, MA). Imaging streams were loaded into Matlab using BioFormats (1).

Particle detection and tracking. Particle detection and tracking were performed using u-track (2) (https://github.com/DanuserLab/u-track). The detection and tracking parameters, listed in Tables S1 and S2, were optimized based on the performance diagnostics included in u-track and visual inspection of the resulting detection and tracking. The mean particle localization precision, as estimated during the Gaussian mixture-model fitting step (2), was 20 nm for VEGFR-2 in one-channel streams, and 26 nm and 33 nm for VEGFR-2 and VEGF, respectively, in two-channel

streams. In all the following analyses, only detections and tracks inside the cell mask (determined from the brightfield image as described above) were employed.

Detection parameters		**One-channel imaging**	**Two-channel imaging**	
		VEGFR-2	**VEGFR-2**	**VEGF**
Gaussian standard deviation		1.33 pixels		
Local maxima detection	Use rolling window time-averaging	No	Yes (windows 1 and 3 frames)*	
	α-value for comparison with local background	0.05	0.05 (window 1), 0.1 (window 3)	0.1 (both windows)
Gaussian mixture-model fitting at local maxima	Do iterative Gaussian mixture-model fitting	Yes		
	α-value for residuals test	0.01		0.05
	α-value for amplitude test	0.05		0.1
	α-value for distance test	0.01	0.05	0.1

Table S1: U-track detection parameters (Gaussian Mixture-Model Fitting). Shown are the parameters with non-default values for any of the three conditions, based on u-track Version 2.2.1. *A rolling window of 1 frame implies no time-averaging. A rolling window of 3 frames means averaging over the current frame, the frame before, and the frame after.

Tracking parameters			VEGFR-2 from one- or two-channel imaging
Overall		Do segment merging	Yes
		Do segment splitting	Yes
Frame-to-frame linking cost function		Brownian search radius upper bound	10 pixels
		Multiplication factor for Brownian search radius calculation	4
Gap closing, merging and splitting cost function	General	Brownian search radius upper bound	10 pixels
		Multiplication factor for Brownian search radius calculation	4
		Scaling power to expand Brownian search radius	0.25
		Use nearest neighbor distance to expand Brownian search radius	No
	Merging & splitting	Search radius lower bound	3 pixels
		For an end/start, the possibility of merging/splitting is allowed only if there is no possibility of gap closing	Yes*
	Birth & death	Birth and death cost	Derived from gap closing and merging/splitting cost formulae

Table S2: U-track tracking parameters. Shown are the parameters with non-default values, based on u-track Version 2.2.1.

*As described in (3), limiting merging and splitting events to segment ends and starts that do not have the possibility of gap closing helps with distinguishing between specific interactions and particles passing by each other.

VEGFR-2 mobility analysis. The diffusion coefficient *D* of each VEGFR-2 particle with track duration ≥ 5 frames was calculated from its frame-to-frame displacement and localization precision, as previously described (4). Tracks with duration < 5 frames were not used for mobility analysis.

As described in the main text, *D* followed a bimodal distribution under all conditions (Fig. 5A). Thus, each VEGFR-2 trajectory was classified as either mobile or immobile/confined, based on whether its diffusion coefficient was greater than or less than the classification threshold, respectively. The classification threshold was taken as 0.032 $\mu m^2/s$ for all conditions in one-channel streams (at the trough between the two modes). In the case of two-channel data, the distribution of VEGFR-2 diffusion coefficients was shifted slightly toward higher values, most likely because of the reduced localization precision in these data due to the images' lower signal-to-noise ratio. Thus the classification threshold was shifted to 0.046 $\mu m^2/s$ in two-channel data, to coincide with the trough between the two modes in this condition.

VEGFR-2 assembly state and dissociation rate estimation. The apparent assembly state for the labeled subset of VEGFR-2 molecules was calculated from the particle intensities and their sequence of merging and splitting events as described in (3) (https://github.com/kjaqaman/FISIK). This analysis required the mean intensity of an individual fluorophore, which was estimated per imaging stream by decomposing the distribution of detected particle intensities in the first 5 frames of the stream into a superposition of multiple modes corresponding to 1, 2, 3, etc. fluorophores (5). Each mode was taken as a log-normal distribution, where the mean and standard deviation of mode n were (approximately) n times those of mode 1 (6). The fit was achieved using least squares, and the number of modes was determined using the Bayesian Information Criterion for model selection (7). With this, the mean individual fluorophore intensity was obtained per imaging stream, and then used to estimate the assembly state of each particle as described in (3). The dissociation rate per assembly state was then calculated from the transitions between assembly states as described in (3).

Analysis of VEGF-VEGFR-2 association in two-channel imaging streams. VEGF-VEGFR-2 association was determined in two steps:

First, in each frame, the colocalization between VEGFR-2 and VEGF particles was determined by solving a linear assignment problem (8) based on their relative positions, with a maximum allowed distance of 4 pixels (~350 nm). This maximum distance accounted for both the particles' localization precision (0.3-0.4 pixels on average) and the 1-3 pixel registration shift between the two cameras acquiring the two-channel images. After this first step, each VEGFR-2 track had a 1/0 association flag with VEGF per frame.

Second, the association history per track was used to distinguish spurious associations from reliable ones. Specifically, a VEGFR-2 track was considered to reliably associate with VEGF if the association history satisfied the following two conditions: (i) Its association flag = 1 in at least three frames. (ii) Its association flag = 1 for at least 10% of the frames between its first frame of VEGF association and last frame of VEGF association (e.g., if the first frame of VEGF association is frame 11, and the last frame of VEGF association is frame 50, then the association flag should be 1 for at least $0.1 \times 40 = 4$ frames). For tracks considered to reliably associate with VEGF, the average fraction of time associated with VEGF was 57% of their duration (34% of the tracks were associated with VEGF for 90% of their duration).

With this, each VEGFR-2 trajectory reliably associated with VEGF was divided into the interval before VEGF association and the interval during VEGF association for further analysis as needed (e.g. VEGFR-2 mobility). Note that if the VEGF-VEGFR-2 association was lost in some later frame, a VEGFR-2 track would then also have an interval after VEGF association, but this was not used for any analysis in our study.

Time-course analysis: data aggregation strategies. For time course analysis, two data aggregation strategies were taken, based on the amount of data available per individual cell to calculate the single-molecule property of interest.

Strategy 1. For single-molecule properties with sufficient data points per cell, primarily properties related to receptor mobility, single-molecule properties were calculated per cell (e.g. mean D_{mobile} per cell), and then individual cell measurements were grouped by time interval for time course analysis. A time interval of 5 minutes was used, as it provided enough individual cell measurements per time interval (10-20) to minimize measurement noise, while allowing for sufficient temporal sampling to capture temporal trends. In this case, the figures display the individual cell measurements, and the mean value and standard error of the mean for the grouped cells per time interval (e.g. Fig. 3C).

Strategy 2. For single-molecule properties with insufficient data points per cell, particularly properties related to receptor interactions (as seen in Fig. 3F, the rate of merging is on the order to 10^{-5}/s/particle), the individual cell measurements could exhibit relatively large fluctuations from cell to cell. In this case, the grouping was done at the level of the tracks within the cells of interest. Specifically, the single-molecule property (e.g. dissociation rate) was calculated from all the tracks combined, and the standard deviation of that property was calculated via bootstrapping (using 100 bootstrap samples). This standard deviation was equivalent to the standard error of the mean of individual cell measurements. In this case, the figures display the property as calculated from the combined tracks and the standard deviation from bootstrapping (e.g. Fig. 2C or Fig. 4B).

Note that, when such analysis was performed on unstimulated cells, all cells were grouped together, as VEGFR-2 properties did not vary over time in that case (e.g. Fig. 3C and Fig. 4E). On

the other hand, when such analysis was performed on stimulated cells, a time interval of 10 minutes was used, thus separating the early and late trends in VEGFR-2 behavior upon VEGF addition (0-10 min and 10-20 min after VEGF addition, respectively). A 10 minute time interval was used instead of a 5 minute time interval (as done above) in order to further reduce measurement noise.

Statistical tests. For properties where individual cell measurements were available in the time course analysis, the properties were compared between conditions for each time interval using a one-sided t-test (based on the individual cell measurements within the time interval). In this case, significant differences are indicated by asterisks above each time interval (e.g. Fig. 3C).

In cases where all per-interval comparisons were not significant (p-value > 0.05), the full time course was compared between conditions using a paired, one-sided t-test. Specifically, each time course was represented by its series of mean values per time interval, and the series of two conditions were compared using a paired t-test. In other words, time courses without VEGF stimulation had 5 data points (e.g. Fig. 5B), while time courses with VEGF stimulation had 4 data points (corresponding to the time intervals after VEGF addition; e.g. Fig. 5C). In this case, significant differences are indicated by a square bracket and an asterisk at the end of the time course plot (e.g. Fig. 5B). The reasoning behind this test was that temporal persistence in a trend (e.g. one condition being always higher than the other) might indicate a significant difference, even if the difference is not strong enough to detect on a per time interval basis.

For properties calculated by first combining all tracks for a group of cells, the property standard deviation was obtained via bootstrapping, and was equivalent to the standard error of the mean of individual cell measurements. In this case, to compare conditions (or time intervals) 1 and 2, with property values μ_1 and μ_2, and variances v_1 and v_2, the difference between them, $\mu_1 - \mu_2$,

was taken to follow $N(0, v_1+v_2)$. This distribution was then used to calculate the p-value to assess the difference between the two conditions (or time intervals). In this case, significant differences are indicated by asterisks above each time interval in the time course (e.g. Fig. 4C), or otherwise as described in the figure legends.

SI Figures

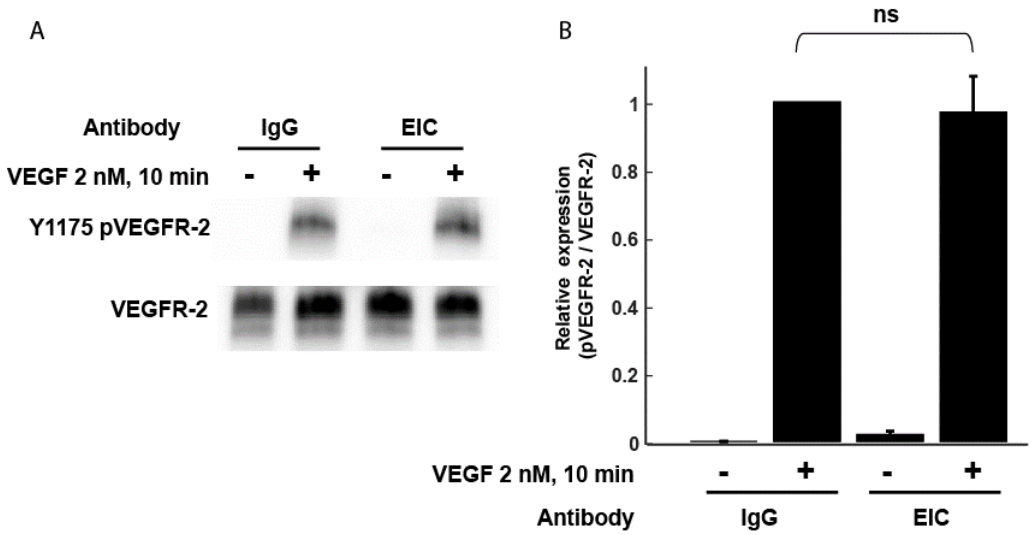

Figure S1. Validation of anti-VEGFR-2 EIC-Fab fragments. (A) Representative Western blot from HDMECs incubated for 4 h in the presence of 5 µg/ml of either nonspecific IgG1 or the anti-VEGFR-2 monoclonal antibody EIC, and stimulated or not with 2 nM VEGF for 10 minutes. Expression of phosphorylated VEGFR-2 (Y1175 pVEGFR-2) and total VEGFR-2 were detected, as described in Materials and Methods. **(B)** Phosphorylated VEGFR-2 expression relative to total VEGFR-2 expression, measured by densitometry, from N = 4 Western blot repeats. Error bars: standard error of the mean. No significant difference was observed between cells treated with IgG1 or EIC antibodies (ns: not significant ($p > 0.05$, Student's t-test)).

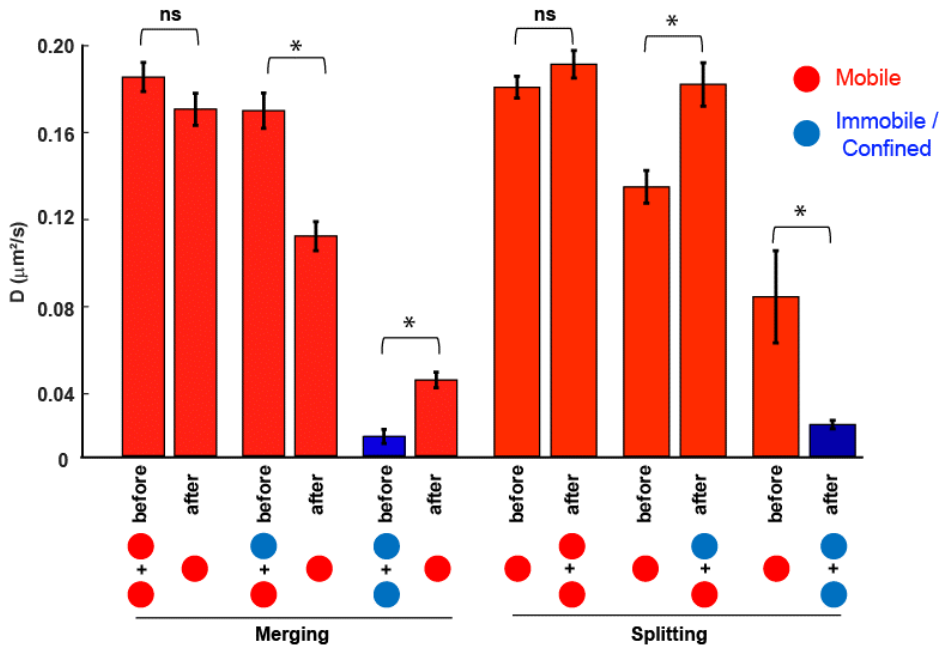

Figure S2. Comparison of VEGFR-2 diffusion coefficients before and after merging or splitting events in unstimulated cells. The results shown are for merging events that produced a mobile particle, and for splitting events that originated in a mobile particle. The purpose was to investigate how merging and splitting events might alter the diffusion coefficient of mobile particles. Red filled circles and bars indicate mobile mode; blue filled circles and bars indicate imm/conf mode. If the two particles before merging/after splitting have the same mobility mode (both mobile or both imm/conf), the shown diffusion coefficient is the average of their two diffusion coefficients. If one particle is mobile and the other is imm/conf, then only the mobile particle diffusion coefficient is shown. Error bars: standard deviations from 100 bootstrap samples. Asterisks and ns (not significant): p-value < 0.005 and p-value > 0.05, respectively (assuming normal distributions with standard deviations obtained by bootstrapping). The comparisons indicate that there is a significant decrease/increase in diffusion coefficient upon merging/splitting only when the merge/split involve one mobile particle and one imm/conf particle. N same as in Fig. 1.

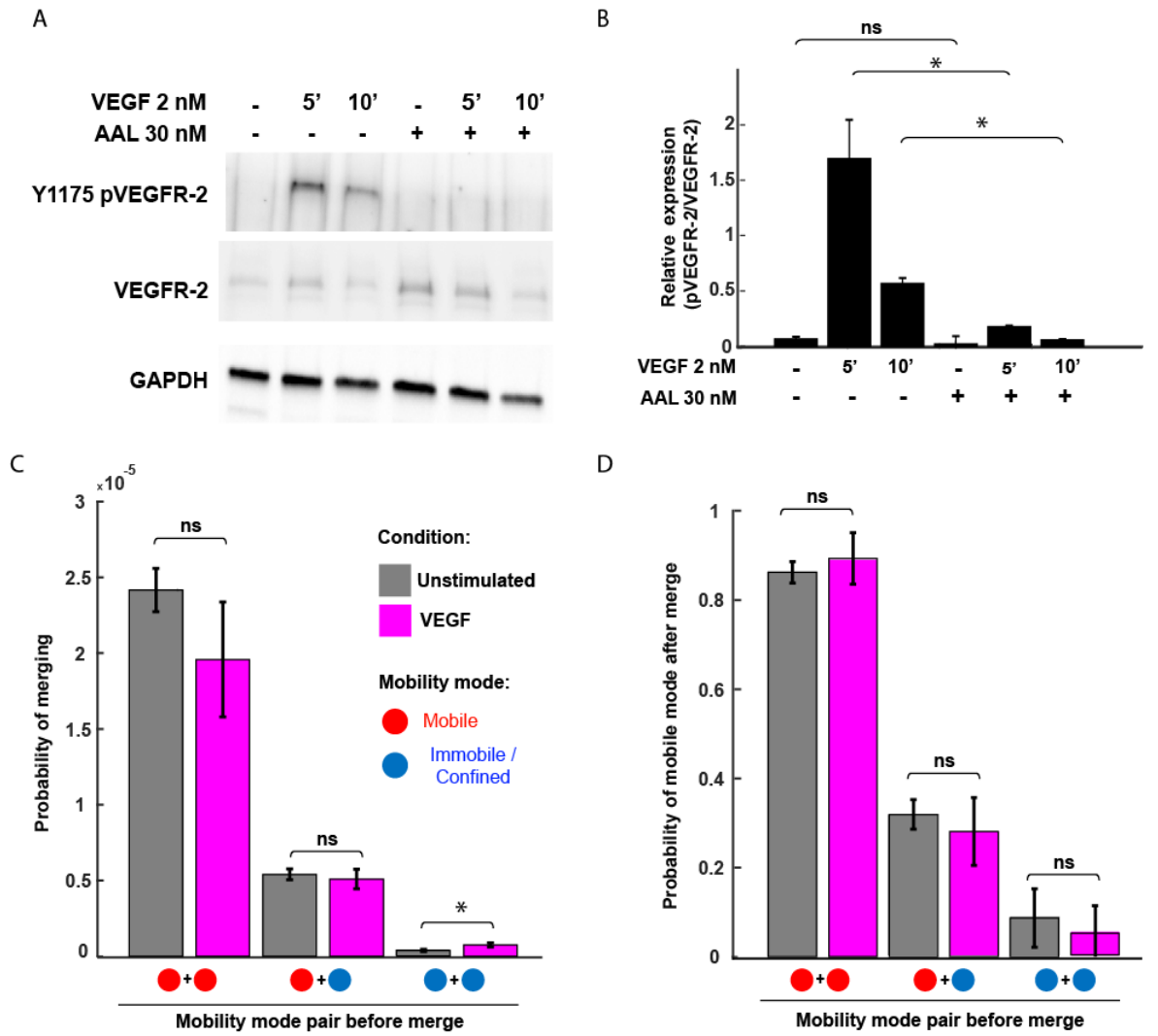

Figure S3. Effect of VEGF and AAL-993 on VEGFR-2 phosphorylation and effect of VEGF on VEGFR-2's merging behavior. (A) Representative Western blot from HDMECs stimulated or not with 2 nM VEGF for 5 or 10 minutes, in the presence or not of the VEGFR-2 phosphorylation inhibitor AAL-993 (treatment with 30 nM for 1 h). Expression of phosphorylated VEGFR-2 (Y1175 pVEGFR-2), total VEGFR-2, and GAPDH were detected, as described in Materials and Methods. **(B)** Phosphorylated VEGFR-2 expression relative to total VEGFR-2 expression, measured by densitometry, from N = 3 Western blot repeats. Error bars: standard error of the mean. Asterisks and ns (not significant): p-value < 0.05 and p-value > 0.05, respectively (Student's t-test). As expected, VEGF leads to significant VEGFR-2 phosphorylation within 5 min, and this is largely abolished in the presence of AAL-993.

Figure S3 (cont.). Effect of VEGF and AAL-993 on VEGFR-2 phosphorylation and effect of VEGF on VEGFR-2's merging behavior. (C) Probability of VEGFR-2 merging per combination of mobility modes before the merge, in cells stimulated (magenta) or not (gray) with 2 nM VEGF for 10-20 min. Error bars: standard deviations from 100 bootstrap samples. Asterisks and ns (not significant): p-value < 0.05 and p-value > 0.05, respectively, when comparing between the indicated conditions (assuming normal distributions with standard deviations obtained by bootstrapping). These comparisons indicate that only the merging probability of two imm/conf particles increases upon VEGF stimulation, while the probabilities of merges involving mobile particles do not change significantly. **(D)** Probability of a merge resulting in a mobile VEGFR-2 particle based on the combination of mobility mode pairs before merging, in cells stimulated or not with 2 nM VEGF for 10-20 min. Colors, error bars and ns same as in (C). N for (C-D) as in Fig.3.

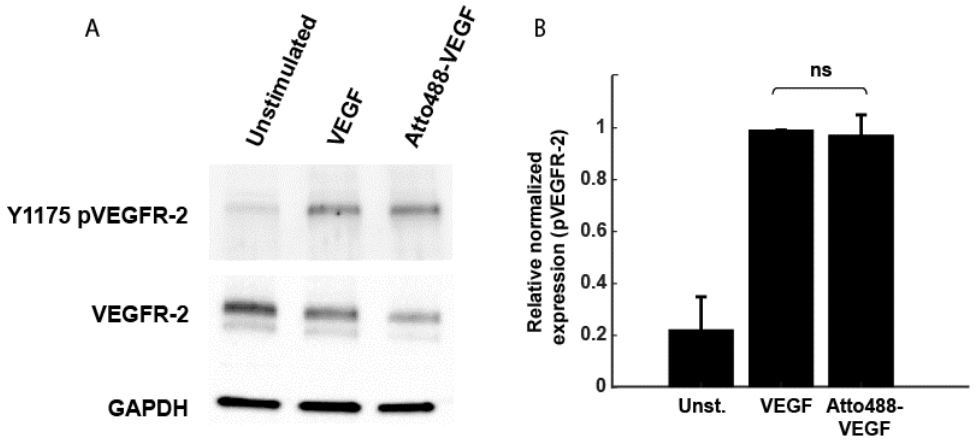

Figure S4. Validation of Atto-488 labeled VEGFA (Atto488-VEGF). (A) Representative Western blot from HDMECs stimulated or not with 2nM VEGF or 2 nM Atto488-VEGF (of which 40% is actually labeled) for 5 minutes. Expression of phosphorylated VEGFR-2 (Y1175 pVEGFR-2), total VEGFR-2, and GAPDH were detected, as described in Materials and Methods. **(B)** Relative normalized expression of phosphorylated VEGFR-2, measured by densitometry, from N = 3 Western blot repeats. Error bars: standard error of the mean. No significant difference was observed between cells treated with VEGF or Atto488-VEGF (ns: not significant (p > 0.05, Student's t-test)).

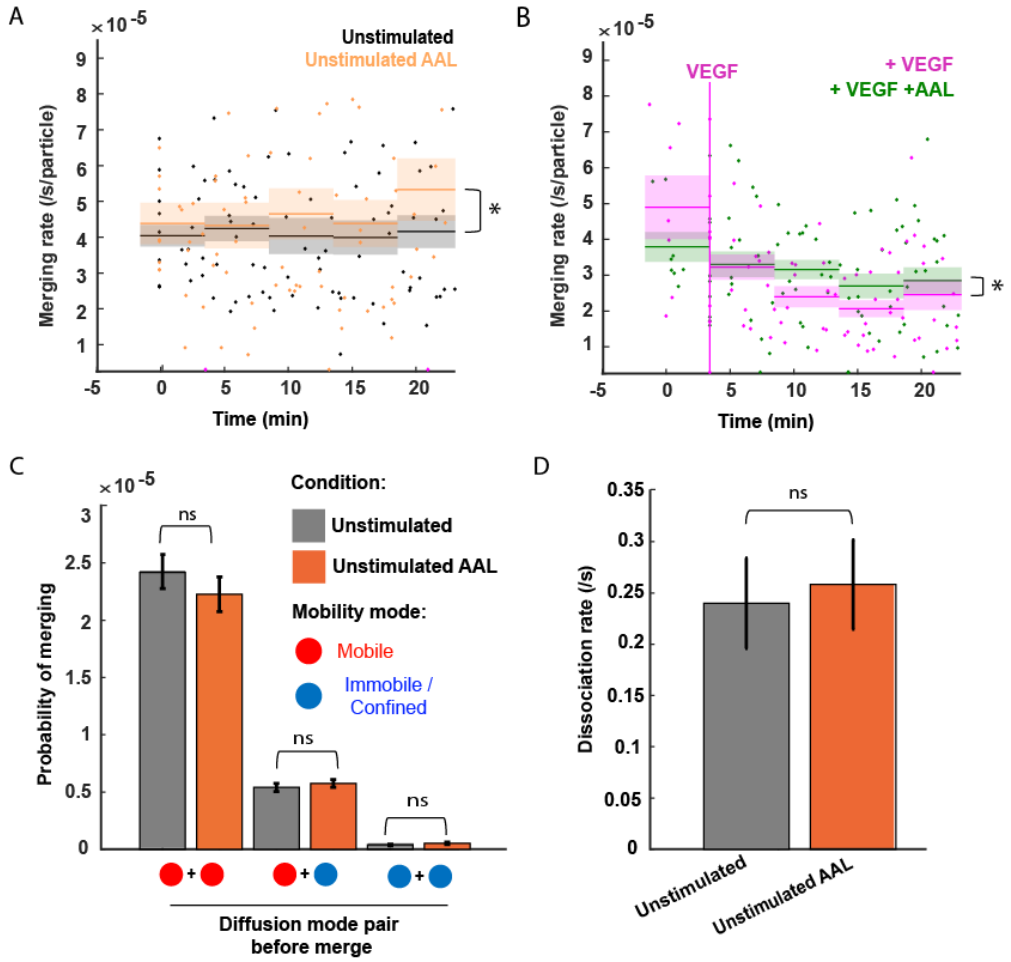

Figure S5. Effect of AAL-993 on the merging and splitting behavior of VEGFR-2. (A-B) Time courses of the merging rates in unstimulated cells in the absence (black) or presence (orange) of 30 nM AAL-993 **(A)**, or in cells stimulated with 2 nM VEGF in the absence (magenta) or presence (green) of 30 nM AAL-993 **(B)**. Dots, lines and surrounding shaded areas, and vertical magenta line as in Fig. 3C-F. Asterisks: p-value < 0.03 for comparing the total time course between conditions using a paired t-test (in (B) the comparison is only for the time intervals after VEGF addition). **(C)** Probability of VEGFR-2 merging per combination of mobility mode pairs before the merge, in unstimulated cells treated (orange) or not (gray) with 30 nM AAL-993. Error bars: standard deviations from 100 bootstrap samples. Ns (not significant): p-value > 0.05 when comparing between the indicated conditions (assuming normal distributions with standard deviations obtained by bootstrapping). These comparisons show no significant differences between treated and untreated cells. **(D)** VEGFR-2 dissociation rate in unstimulated cells treated (orange) or not (gray) with 30 nM AAL-993. Error bars and ns as in (C). There is no significant difference between treated and untreated cells. N as in Fig. 5.

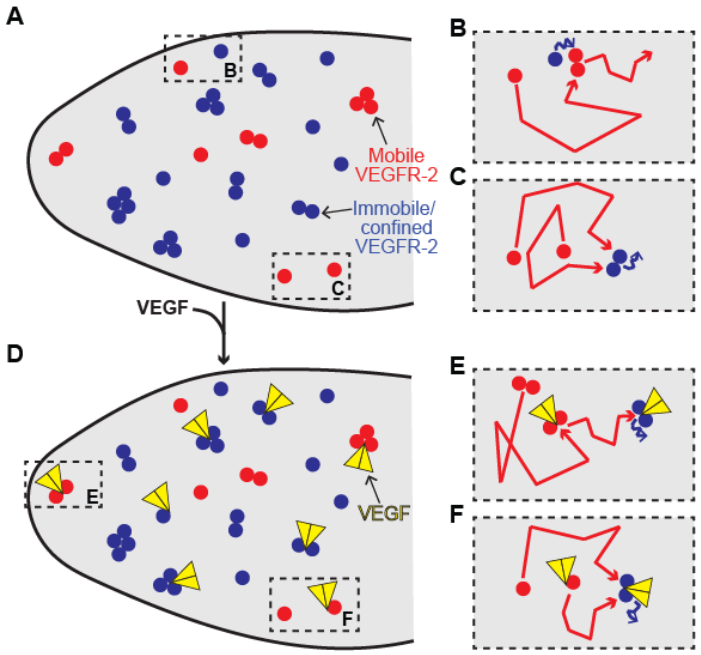

Figure S6. Schematic of VEGFR-2 spatiotemporal organization and its relationship to VEGF. (A) In unstimulated cells, VEGFR-2 can be mobile (red; ~35%) or imm/conf (blue; ~65%), and has a distribution of assembly states, with more imm/conf molecules than mobile molecules in non-monomeric states. Boxed regions are used to illustrate examples of the interplay between mobility and interactions in (B-C). **(B-C)** Example illustrations of one mobile monomer and one imm/conf monomer associating to produce a mobile dimer **(B)**, and of two mobile monomers associating to produce an imm/conf dimer **(C)**. The examples illustrate a sequence of events, showing the molecules when separate (separate dots) and upon interacting with each other (paired-dots). The dot colors reflect the molecules' mobility mode moving forward. Molecule movement is indicated by jagged lines colored by mobility mode, with arrows indicating direction of movement. While these two examples are not comprehensive, they reflect that the mobile mode promotes interactions, which in turn enrich the imm/conf mode, but without a simple one-to-one relationship between mobility and assembly state. (D) VEGF binds to VEGFR-2 monomers and pre-existing non-monomers, and stabilizes the non-monomeric state (not illustrated). VEGF symbol is not drawn to scale. Boxed regions are used to illustrate examples of the interplay between VEGF binding and VEGFR-2 mobility and interactions (E-F). **(E-F)** Example illustrations of VEGF binding to a pre-existing mobile dimer, such that the ligated dimer slows down and eventually switches mobility to imm/conf **(E)**, and of VEGF binding to a mobile monomer, which then associates with an unligated mobile monomer, producing a ligated imm/conf dimer. The illustration style follows that in (B-C). Again, while these two examples are not comprehensive, they reflect that VEGF can bind monomeric and non-monomeric VEGFR-2 and that VEGF binding slows down mobile VEGFR-2 and promotes the imm/conf mode of VEGFR-2 mobility, which depends on VEGFR-2 phosphorylation (not illustrated).

Movie legends

Movie 1: Single-molecule imaging of endogenous VEGFR-2 in primary HDMECs. Representative 10 Hz single-molecule imaging stream of an unstimulated cell. The first 10 s of the 20 s stream are shown. Image size is 45.5 × 45.5 μm^2.

Movie 2: VEGFR-2 particle tracking. Same single-molecule imaging stream as in Movie 1, with VEGFR-2 tracks overlaid on the fluorescence images. Random track colors are used to help distinguish neighboring tracks.

Movie 3: VEGFR-2 mobility classification. Same VEGFR-2 tracks as in Movie 2, but now color-coded based on mobility mode. Red = mobile; blue = immobile/confined, light pink = too short to classify (duration < 5 frames).

Movie 4: Example VEGFR-2 merging and splitting events. Example is a zoom of an area from same stream shown in Movies 1-3. Image size is 4 × 4.8 μm^2.

Movie 5: Example VEGFR-2 merging and splitting events. Example is from a different single-molecule imaging stream of VEGFR-2. Image size is 3.2 × 3.6 μm^2.

Movie 6: Example of a VEGFR-2 particle associated with a VEGF particle. Example is from a 10 Hz/20 s simultaneous two-channel TIRF imaging stream of VEGFR-2 labeled with RRX (left image) and Atto488-VEGF (right image). The VEGFR-2 track is overlaid on both images as a red

circle followed by a light pink dragtail, while the associated VEGF particle is overlaid on the right image as a cyan circle. Image size is $3.2 \times 3.2\ \mu m^2$.

References

1. Linkert M, *et al.* (2010) Metadata matters: access to image data in the real world. *J. Cell Biol.* 189(5):777-782.
2. Jaqaman K, *et al.* (2008) Robust single-particle tracking in live-cell time-lapse sequences. *Nat Methods* 5(8):695-702.
3. De Oliveira LR & Jaqaman K (2019) FISIK: Framework for the Inference of In Situ Interaction Kinetics from Single-Molecule Imaging Data. *Biophys J* 117(6):1012-1028.
4. Jaqaman K, Galbraith JA, Davidson MW, & Galbraith CG (2016) Changes in single-molecule integrin dynamics linked to local cellular behavior. *Mol Biol Cell* 27(10):1561-1569.
5. Jaqaman K, *et al.* (2011) Cytoskeletal control of CD36 diffusion promotes its receptor and signaling function. *Cell* 146(4):593-606.
6. Mutch SA, *et al.* (2007) Deconvolving single-molecule intensity distributions for quantitative microscopy measurements. *Biophysical Journal* 92(8):2926-2943.
7. Jaqaman K & Danuser G (2006) Linking data to models: data regression. *Nat. Rev. Mol. Cell Biol.* 7(11):813-819.
8. Jonker R & Volgenant A (1987) A Shortest Augmenting Path Algorithm for Dense and Sparse Linear Assignment Problems. *Computing* 38(4):325-340.